Received 23 December 2025; accepted 12 January 2026. Date of publication 20 January 2026; date of current version 26 March 2026.

Digital Object Identifier 10.1109/OJAP.2026.3656343

A Divide-and-Conquer Tiling Method for the Design of Large Aperiodic Phased Arrays

NICOLA ANSELMI [1] (Senior Member, IEEE), PAOLO ROCCA [2,3,4] (Fellow, IEEE), GIOVANNI TOSO [5] (Fellow, IEEE), AND ANDREA MASSA [2,6,7,8] (Fellow, IEEE)

[1]Université de Rennes, Institut d'Électronique et des Technologies du Numérique (IETR) UMR 6164, 35000 Rennes, France
[2]ELEDIA Research Center (ELEDIA@UniTN - University of Trento), DICAM - Department of Civil, Environmental, and Mechanical Engineering, 38123 Trento, Italy
[3]ELEDIA Research Center (ELEDIA@XIDIAN - Xidian University), 710071 Xi'an, Shaanxi Province, China
[4]ELEDIA Research Unit, CNIT - University of Trento, 38123 Trento, Italy
[5]Antenna and Submillimeter Wave Section, Radio Frequency Payloads and Technology Division, European Space Agency (ESA-ESTEC), 2200 AG Noordwijk, The Netherlands
[6]ELEDIA Research Center (ELEDIA@UESTC - UESTC), School of Electronic Science and Engineering, University of Electronic Science and Technology of China, Chengdu 611731, China
[7]ELEDIA Research Center (ELEDIA@TSINGHUA - Tsinghua University), Beijing 100084, China
[8]School of Electrical Engineering, Tel Aviv University, Tel Aviv 69978, Israel

CORRESPONDING AUTHOR: ANDREA MASSA (e-mail: andrea.massa@unitn.it)

This work was supported in part by the networking activities carried out within the Project DICAM-EXC funded by the Italian Ministry of Education, Universities and Research (MUR) within the "Departments of Excellence 2023–2027" Program (CUP: E63C22003880001) under Grant L232/2016, in part by the Project "AURORA - Smart Materials for Ubiquitous Energy Harvesting, Storage, and Delivery in Next Generation Sustainable Environments" funded by the Italian Ministry for Universities and Research within the PRIN-PNRR 2022 Program (CUP: E53D23014760001), in part by the National Natural Science Foundation of China under Grant U25A20300, and in part by the Natural Science Basic Research Program of Shaanxi Province under Grant 2024JC-ZDXM-25.

ABSTRACT Due to the growing demand from modern wireless applications of cost-affordable and high-gain scanning antenna solutions, the design of large phased arrays (PAs) with radiating elements organized into modular clusters with sub-array-only amplitude and phase control is a key topic. In this paper, an innovative irregular tiling method is proposed where, according to a divide-and-conquer strategy, the antenna aperture is subdivided into sub-areas that are locally domino-tiled by jointly fulfilling the full-coverage condition on the remaining untiled part of the PA support. Selected representative results, including comparisons with competitive state-of-the-art synthesis methods, are reported to prove the effectiveness and the computational scalability for large PAs of the proposed tiling approach. Use-cases of current relevance for low Earth orbit (LEO) satellite communications are discussed, as well, to provide the antenna designers useful practical guidelines for handling large PAs.

INDEX TERMS Phased array, large array antenna, sub-array, tiling, domino, optimization-based synthesis, satellite communications.

I. INTRODUCTION

PHASED array (*PA*) antennas are nowadays a widespread technology, but still complex and expensive for space-based communication services based on low-orbit satellites. Indeed, antenna solutions for fixed/mobile ground stations or in space satellites [1] require wide beam steering angles and high gains, while large apertures, filled by thousands of radiating elements, imply too high implementation costs. An effective way to reduce the *PA* architecture complexity, the antenna weight, and the power consumption is that of making the array layout highly modular so that the antenna fabrication and its deployment become easier, scalable [2], and the number of amplifiers and phase shifters is reduced, as well. Towards this end, unconventional *PA*s (e.g., clustered layouts) have been deeply investigated [3] even though the reduction of the amplitude and phase controls generally causes the appearance of grating lobes and the presence of high quantization lobes, whose intensity and number grow with the average electrical size of the clusters and the scan angle [4], [5], [6]. To cope with these problems, the aperiodic

arrangement of the sub-array phase centers turns out to be a reliable strategy as proven in the seminal works [4], [7]. Therefore, several approaches to the synthesis of irregularly clustered arrays have been proposed [8], [9], [10], [11], [12], [13], [14], [15], [16], [17], [18], [19], [20], [21], [22] where polyomino shaped tiles [8], [9], [10], [11], [12], [13], tile panels characterized by sparse [14] or clustered [15] arrangements of the array elements within the tiles, flipped regular sub-arrays [16], diamond or Penrose-inspired sub-array partitions [17], [18] or different tile sizes [19] have been used.

In the recent literature, the most investigated polyomino shape is the *domino* one [11], [12], [13], [20], [21], [22] where two elementary pixels are horizontally or vertically grouped in a rectangular shape. A domino building block presents several positive features such as the full coverage of rectangular as well as arbitrary orthogonal-polygon like apertures [12], while affording sub-array layouts suitable for an easy fabrication and assembly. Moreover, domino tiling avoids half transmit-receive modules (*TRM*s) of a fully-populated (*FP*) array still guaranteeing an adequate clustering ratio for fulfilling challenging radiation requirements. Furthermore, only two types of tiles, namely the vertical domino and the horizontal one, are needed to fit user-desired polarization states, unless the circular polarization case for which the dominoes can be all equal [11].

Dealing with domino clustering, customized tiling theorems have been introduced to state the necessary conditions for the full coverage of the antenna aperture in case of rectangular [11] and arbitrary orthogonal-polygon [12] arrays. Enumerative [11] or optimization-driven [12] techniques have been developed for determining the best tiling when dealing with small- or medium-size arrays, respectively. Moreover, domino-tiled *PA*s with time-dependent control points [13] have been proposed, as well, or the maximization of the peak directivity [21], [22] has been yielded by means of entropy-based optimization techniques. However, all these methods suffer either a slow convergence or too high computational costs since not scalable for addressing the synthesis of very large arrays, which is the typical case of modern satellite services where stringent regulatory pattern masks need to be satisfied and high gains are required.

Despite the use of arbitrary polyominoes and without any restriction on the number of copies of each tile shape, only small- and medium-size *PA*s have been optimally synthesized in [23] by means of an exact method based on a branch-and-bound strategy. Otherwise, heuristic approaches have been implemented to handle wider *PA*s, but yielding sub-optimal tile arrangements.

This paper deals with the synthesis of large *PA*s with domino tiles by means of an innovative computationally-scalable method based on a "divide and conquer" strategy. Starting from a reference *FP* array layout, the antenna aperture is partitioned into multiple and contiguous smaller sub-regions that are iteratively domino tiled, in optimal way through analytic rules, by still fulfilling the full-coverage (i.e., without holes) condition on the untiled remaining part of the array [24]. To enhance the irregularity of the arising tilings, thus enabling enhanced radiation performance thanks to a more exhaustive exploration of the solution space, soft boundaries have been implemented among adjacent sub-regions to allow the inclusion in a domino of two radiating elements not belonging to the same partition.

To the best of the authors' knowledge, the main novelties of our research work over the existing literature comprise (*i*) a customized method for the optimal tiling of large *PA*s using domino-shaped sub-arrays where, according to a divide-and-conquer strategy, the antenna aperture of a reference *FP PA* is subdivided into small and contiguous regions that are locally tiled, while the radiation performance on the whole array layout are evaluated, (*ii*) a suitable use of analytic theorems for determining, sequentially and exploiting soft-boundary concepts, the optimal tiling of each sub-aperture by jointly fulfilling the full coverage condition for the remaining untiled area of the *PA* aperture, and (*iii*) the derivation of engineering guidelines for the use of the proposed method to handle large *PA*s.

The rest of the paper is organized as follows. The mathematical formulation of the synthesis of domino-tiled arrays is summarized in Section II by firstly defining the tiling problem at hand (Section II-A) and then (Section II-B) describing the proposed "divide and conquer" tiling method. Representative numerical examples, including benchmark comparisons with competitive state-of-the-art tiling methods and test cases of current practical relevance in *LEO* satcom applications, are reported in Section III. Eventually, some conclusions and final remarks are drawn (Section IV).

II. MATHEMATICAL FORMULATION

A. PROBLEM FORMULATION

Let us consider a planar rectangular *PA* with radiating elements arranged on a rectangular lattice laying on the (x, y)-plane, d_x and d_y being the inter-element spacing along the x- and the y- axis, respectively (Fig. 1). Each element is assumed to belong to a square unit cell, namely a *pixel,*[1] such that the antenna aperture $\mathcal{A}$ turns out composed of M columns and N rows, either M or N being even to fulfill the full-coverage condition of $\mathcal{A}$ with domino tiles [11]. The *EM* field radiated in far-field by the array is given by

$$\mathbf{F}(u, v) = \sum_{m=1}^{M} \sum_{n=1}^{N} \mathbf{g}_{mn}(u, v) w_{mn} e^{j\frac{2\pi}{\lambda}(x_m u + y_n v)} \qquad (1)$$

where $\mathbf{g}_{mn}(u, v)$ is the active/embedded element pattern [5] of the (m, n)-th $(m = 1, \ldots, M;\ n = 1, \ldots, N)$ radiating element centered at (x_m, y_n) with complex excitation w_{mn} $(w_{mn} = \alpha_{mn} e^{j\beta_{mn}}$, α_{mn} and β_{mn} being the corresponding amplitude and phase coefficient, respectively). Moreover, λ

[1]For the sake of notation simplicity, each pixel is supposed to include only one radiating element. However, each pixel is a logical unit cell that can include one or more radiating elements without loss of validity of the proposed tiling method.

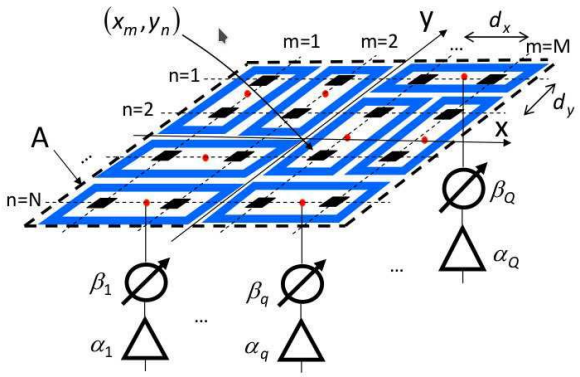

FIGURE 1. Sketch of a domino-tiled *PA* layout.

is the wavelength at the antenna carrier frequency, $u = \sin\theta\cos\phi$ and $v = \sin\theta\sin\phi$ are the cosine angular directions, (θ, ϕ) being the angular variables.

To simplify the array architecture, the $M \times N$ array elements are clustered into Q ($Q \triangleq \frac{M\times N}{2}$) domino tiles so that each pixel belongs to a domino and the aperture $\mathcal{A}$ is entirely covered. At the sub-array level, each tile is connected to a single *TRM* (Fig. 1) and the equivalent (m, n)-th ($m = 1, \ldots, M$; $n = 1, \ldots, N$) element-level excitation can be expressed in terms of the q-th ($q = 1, \ldots, Q$) sub-array weight as follows

$$w_{mn} = \sum_{q=1}^{Q} \delta_{c_{mn}q}\alpha_q e^{j\beta_q} \tag{2}$$

($\widehat{\mathbf{w}}$ being the corresponding complex excitation vector, $\widehat{\mathbf{w}} \triangleq \{w_{mn};\ m = 1, \ldots, M;\ n = 1, \ldots, N\}$) where $\boldsymbol{\alpha} = \{\alpha_q;\ q = 1, \ldots, Q\}$ and $\boldsymbol{\beta} = \{\beta_q;\ q = 1, \ldots, Q\}$ are the real sub-array amplitude and phase Q-vectors, respectively, $\delta_{c_{mn}q}$ is the Kronecker delta function equal to $\delta_{c_{mn}q} = 1$ when the (m, n)-th ($m = 1, \ldots, M$; $n = 1, \ldots, N$) element belongs to the q-th ($q = 1, \ldots, Q$) domino ($c_{mn} = q$), while $\delta_{c_{mn}q} = 0$ otherwise ($c_{mn} \neq q$), $\mathbf{c} = \{c_{mn};\ m = 1, \ldots, M;\ n = 1, \ldots, N\}$ being the array partitioning vector encoding the aggregation of the $M \times N$ array elements into the Q dominoes.

The synthesis of domino-tiled *PA*s can be then stated as follows:

> *Domino-Tiled PA Synthesis* - Given an array aperture $\mathcal{A}$ of $M \times N$ elements, determine the optimal clustering, $\mathbf{c}^{opt}$, of the array elements into Q domino sub-arrays and the sets of sub-array amplitudes, $\boldsymbol{\alpha}^{opt}$, and phases, $\boldsymbol{\beta}^{opt}$, that minimize the *pattern matching* function
>
> $$\Phi(\mathbf{c}) \triangleq \frac{\int_\Omega [\mathcal{P}(u,v) - \Psi(u,v)] \times \mathcal{H}\{\mathcal{P}(u,v) - \Psi(u,v)\} du dv}{\int_\Omega \Psi(u,v) du dv} \tag{3}$$
>
> where $\mathcal{P}(u, v)$ ($\mathcal{P}(u, v) \triangleq |\mathbf{F}(u, v)|^2$) is the power pattern radiated by the domino-tiled *PA*, $\Psi(u, v)$ is a positive upper-bound mask defined by the user over the angular domain Ω ($\Omega \triangleq \{(u, v) \mid u^2+v^2 \leq 1\}$), and $\mathcal{H}$ is the Heaviside step function.

Such a synthesis problem is handled in Section II-B by means of an innovative method suitable for large *PA*s, as well.

B. DIVIDE AND CONQUER TILING METHOD

The synthesis of domino-tiled *PA*s has been already addressed in [11] by means of an exhaustive tiling strategy, named enumerative tiling method (*ETM*), able to find the optimal solution since iteratively exploring the whole solution space of the T admissible clustered configurations, $\mathbf{C} = \{\mathbf{c}^{(t)};\ t = 1, \ldots, T\}$. Unfortunately, the *ETM* is realistically applicable only to small arrays because of its computational cost. Therefore, the optimization-based tiling method (*OTM*) has been proposed in [11] to deal with the synthesis of wider arrays thanks to the effective sampling of the solution space yielded by an *ad-hoc* method based on a schemata-driven Genetic Algorithm (*GA*). However, the synthesis of bigger domino-tiled *PA*s, including thousands of radiating elements, turns out to be unaffordable for the *OTM*, as well. To overcome the dimensionality limitation of current tiling techniques, we propose the divide-and-conquer tiling method (*DCTM*), which is aimed at providing suitable trade-offs between the optimality of the synthesized tiling and the required computational burden. Towards this end, the antenna aperture $\mathcal{A}$ of a reference *FP-PA* is first partitioned into I smaller sub-apertures, $\{\mathcal{S}^{(i)};\ i = 1, \ldots, I\}$ such that $\mathcal{A} = \bigcup_{i=1}^{I} \mathcal{S}^{(i)}$ and $\mathcal{S}^{(i)} \cap \mathcal{S}^{(j)} = 0$ ($i, j = 1, \ldots, I$; $i \neq j$). Then, each i-th ($i = 1, \ldots, I$) array sub-region, $\mathcal{S}^{(i)}$, is progressively tiled using dominoes and assuming soft-boundaries with the adjacent partitions to build dominoes with two close radiating elements, but not exactly laying in the same $\mathcal{S}^{(i)}$.

More in detail, the *DCTM* is implemented through the sequence of the following steps:

STEP 1 - ARRAY APERTURE SETUP AND REFERENCE PATTERN SELECTION

- *Step 1.1 - Array Aperture Setup*. Let the pixels of the aperture $\mathcal{A}$ be mapped in the checkerboard pattern shown in Fig. 2(a). By grouping the set of external and internal vertices into the vectors $\bar{\mathbf{v}} = \{\bar{v}_b;\ b = 1, \ldots, B\}$ [$B \triangleq 2\times(M+N)$] ($\bar{v}_b \in \partial\mathcal{A}$, $\partial\mathcal{A}$ being the periphery of $\mathcal{A}$) and $\mathbf{v} = \{v_l;\ l = 1, \ldots, L\}$ [$L \triangleq (M-1)\times(N-1)$], respectively, let (v_l, v_r) be a generic edge connecting the vertex v_l to the vertex v_r and let us assume the edges of the white(grey) pixels oriented clockwise(counter-clockwise) [Fig. 2(a)];
- *Step 1.2 - Height Function Computation*. For each b-th ($b = 1, \ldots, B$) external vertex, $\bar{v}_b$, compute the corresponding value of the height function (*HF*), $\bar{h}_b$ ($\bar{h}_b \triangleq h(\bar{v}_b) \rightarrow \bar{\mathbf{h}} = \{\bar{h}_b;\ b = 1, \ldots, B\}$) [25] by nullifying the *HF* value of the first ($b = 1$) vertex on the top left corner of the aperture ($\bar{h}_b|_{b=1} = 0$) and

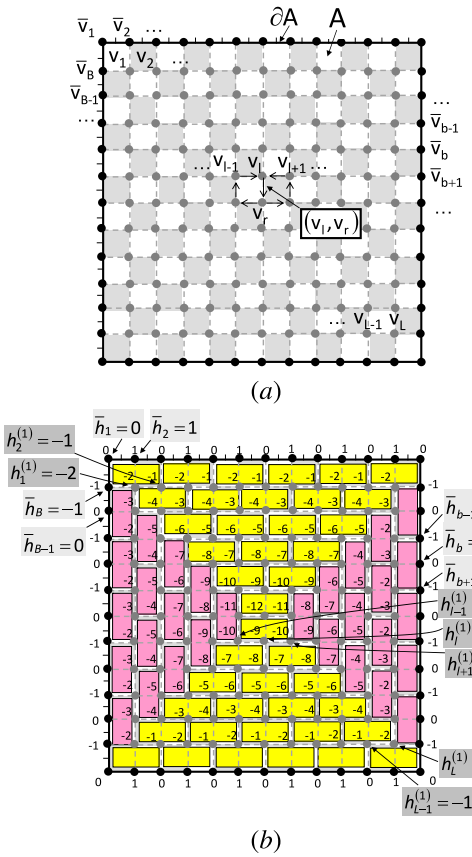

FIGURE 2. *Illustrative Example* ($M = N = 12$) - Sketch of (a) the checkerboard pattern of the array aperture $\mathcal{A}$ together with the external/internal vertices and the edges and (*b*) the *minimal* (domino) *tiling* of $\mathcal{A}$ including the values of the *HF* on the vertices.

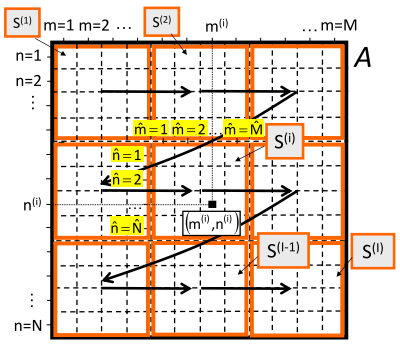

FIGURE 3. *Illustrative Example* ($M = N = 12$; $I = 9$) - Sketch of the partition of the array aperture $\mathcal{A}$ into I sub-areas, $\{\mathcal{S}^{(i)}; i = 1, \ldots, I\}$.

then determining the *HF* values of the remaining $B-1$ vertices ($b = 2, \ldots, B$) as follows

$$\bar{h}_b = \begin{cases} \bar{h}_{b-1} + 1 & \text{if } \exists\ (\bar{v}_{b-1},\ \bar{v}_b) \\ \bar{h}_{b-1} - 1 & \text{if } \exists\ (\bar{v}_b,\ \bar{v}_{b-1}) \end{cases} \tag{4}$$

[Fig. 2(*b*)];

- *Step 1.3 - Minimal Tiling Definition*. Define the minimal tiling solution, $\mathbf{c}^{(t)}|_{t=1}$, and the associated *HF* values of the internal vertices, $\mathbf{h}^{(1)} = \mathbf{h}(\mathbf{c}^{(1)})$ [$\mathbf{h} = \{h_l;\ l = 1, \ldots, L\}$, $h_l \triangleq h(v_l)$] [Fig. 2(*b*)] according to the *Algorithm B1* in [11];
- *Step 1.4 - Aperture Partitioning*. Split the aperture $\mathcal{A}$ into I partitions, $\{\mathcal{S}^{(i)};\ i = 1, \ldots, I\}$, of equal size $\widehat{M} \times \widehat{N}$ ($\widehat{M} \leq M$ and $\widehat{N} \leq N$) such that ($M\ mod\ \widehat{M}$) $= 0$ and ($N\ mod\ \widehat{N}$) $= 0$, *mod* being the modulo operation (e.g., Fig. 3 - $M = N = 12$, $\widehat{M} = \widehat{N} = 4$, $I = 9$). The coordinates of the (r, s)-th ($r = 1, \ldots, \widehat{M}$; $s = 1, \ldots, \widehat{N}$) pixel of the i-th ($i = 1, \ldots, I$) sub-aperture, $\mathcal{S}^{(i)}$, are $(x_{\widehat{m}_r}, y_{\widehat{n}_s})$ where $\widehat{m}_r = r + (i - 1 - \frac{\lfloor (i-1) \times \frac{\widehat{M}}{M} \rfloor}{\frac{\widehat{M}}{M}}) \times \widehat{M}$ and $\widehat{n}_s = s + \lfloor (i-1) \times \frac{\widehat{M}}{M} \rfloor \times \widehat{N}$, $\lfloor \cdot \rfloor$ being the floor function;
- *Step 1.5 - Reference Pattern Selection*. Define the set of $M \times N$ amplitude, $\boldsymbol{\alpha}^{ref} = \{\alpha^{ref}_{mn};\ m = 1, \ldots, M;\ n = 1, \ldots, N\}$, and phase, $\boldsymbol{\beta}^{ref} = \{\beta^{ref}_{mn};\ m = 1, \ldots, M;\ n = 1, \ldots, N\}$, coefficients ($\rightarrow \mathbf{w}^{ref} = \{w^{ref}_{mn}; m = 1, \ldots, M;\ n = 1, \ldots, N\}$, $w^{ref}_{mn} \triangleq \alpha^{ref}_{mn} e^{j\beta^{ref}_{mn}}$) of the *FP* array affording a reference pattern, $\mathcal{P}^{ref}(u, v)$, compliant with the user-defined requirements coded by $\Psi(u, v)$;

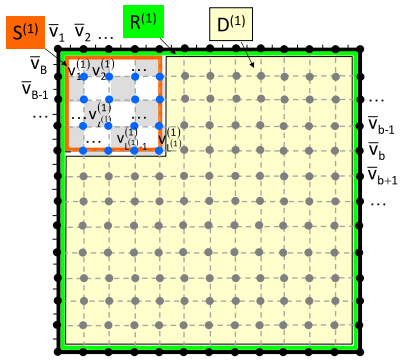

FIGURE 4. *Illustrative Example* ($M = N = 12$; $i = 1$) - Sketches of the partition of $\mathcal{A}$ under *DCTM* domino-tiling, $\mathcal{S}^{(i)}$, the area to be tiled, $\mathcal{R}^{(i)}$, and the remaining area, $\mathcal{D}^{(i)}$ ($\mathcal{D}^{(i)} \triangleq \mathcal{R}^{(i)} - \mathcal{S}^{(i)}$).

STEP 2 - DIVIDE-AND-CONQUER DOMINO TILING OPTIMIZATION

- *Step 2.1 - Initialization*. At the first ($i = 1$) iteration of the *DCTM*, set $\mathcal{R}^{(i)}\rfloor_{i=1} = \mathcal{A}$ [$\mathcal{R}^{(i)}$ ($i = 1, \ldots, I-1$) being the untiled area of $\mathcal{A}$, $\mathcal{R}^{(i)} \triangleq \mathcal{A} - \sum_{j=1}^{i-1} \mathcal{S}^{(j)}$] and $\widehat{\mathbf{w}} = \emptyset$ since the whole aperture has to be tiled and no domino clusters have been used yet, respectively;
- *Step 2.2 - $\mathcal{S}^{(i)}$ Sub-Aperture Tiling*. To generate tiled configurations not only confined to $\mathcal{S}^{(i)}$, but with dominoes that can potentially exceed the boundary between $\mathcal{S}^{(i)}$ and the remaining part of $\mathcal{A}$ to be processed, $\mathcal{D}^{(i)}$ ($\mathcal{D}^{(i)} \triangleq \mathcal{A} - \sum_{j=1}^{i} \mathcal{S}^{(j)} \rightarrow \mathcal{D}^{(i)} = \mathcal{R}^{(i)} - \mathcal{S}^{(i)}$) [light yellow region in Fig. 4 ($i = 1$) and Fig. 5 ($i = 2$)], consider not only the internal vertices of $\mathcal{S}^{(i)}$, but also those laying on the boundary between $\mathcal{S}^{(i)}$ and $\mathcal{D}^{(i)}$, $\widehat{\mathbf{v}} = \{v_{\widehat{l}};\ \widehat{l} = 1, \ldots, L^{(i)}\}$ [blue color dots in Fig. 4 ($i = 1$) and Fig. 5 ($i = 2$)]. Then, if the condition $\eta \leq \eta_{th}$ ($\eta \triangleq \sqrt{\frac{\widehat{M} \times \widehat{N}}{M \times N}}$ and η_{th} being a user-defined

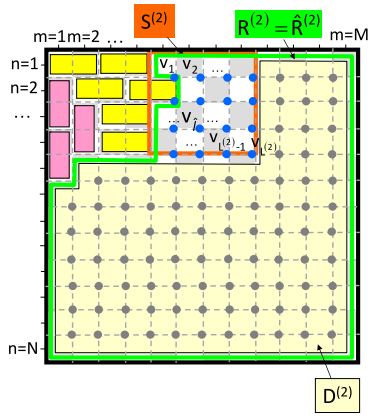

FIGURE 5. *Illustrative Example* ($M = N = 12$; $i = 2$) - Sketches of the partition of $\mathcal{A}$ under *DCTM* domino-tiling, $\mathcal{S}^{(i)}$, the area to be tiled, $\mathcal{R}^{(i)}$, and the remaining area, $\mathcal{D}^{(i)}$ ($\mathcal{D}^{(i)} \triangleq \mathcal{R}^{(i)} - \mathcal{S}^{(i)}$).

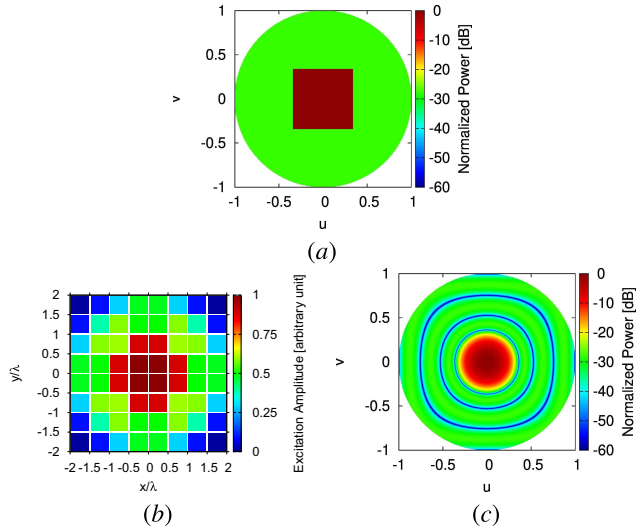

FIGURE 6. *Numerical Validation* ($M = N = 8$, Isotropic Elements, $d_x = d_y = \frac{\lambda}{2}$, $(\theta_0, \phi_0) = (0, 0)$ [deg] [$\rightarrow (u_0, v_0) = (0, 0)$]) - Plots of (a) the power pattern mask, $\Psi(u, v)$, (b) the amplitude distribution of the reference excitations, α^{ref}, and (c) the reference power pattern, $\mathcal{P}^{ref}(u, v)$, in the (u, v)-domain Ω.

switching threshold) holds true, use the *enumerative DCTM* (*E-DCTM*) strategy:

- Assign to the vertices $\widehat{\mathbf{v}}$, the *HF* values, $\widehat{\mathbf{h}}^{(1)} = \{h_{\widehat{l}}^{(1)}; \widehat{l} = 1, \ldots, L^{(i)}\}$, of the minimal tiling, $\mathbf{h}^{(1)}$ (i.e., $h_{\widehat{l}}^{(1)} = h^{(1)}(v_{l \rightarrow \widehat{l}})$ $(\widehat{l} = 1, \ldots, L^{(i)};\ l = 1, \ldots, L)$, where the notation $l \rightarrow \widehat{l}$ indicates the l-th pixel in $\mathcal{A}$ that corresponds to the $\widehat{l}$-th one in $\mathcal{S}^{(i)}$);
- Exhaustively generate all (i.e., including the layouts with dominoes overlapping the soft boundaries of $\mathcal{S}^{(i)}$, as well) tilings of $\mathcal{S}^{(i)}$, $\widehat{\mathbf{C}} = \{\mathbf{c}^{(\widehat{t})}; \widehat{t} = 1, \ldots, T^{(i)}\}$ according to the *ETM* method [11];
- Check the admissibility of each $\widehat{t}$-th $(\widehat{t} = 1, \ldots, T^{(i)})$ trial domino arrangement $\mathbf{c}^{(\widehat{t})}$ by verifying the "*Admissibility Condition*", that is, whether $\mathcal{R}^{(i+1)}$ can be fully covered with dominoes according to the procedure developed for orthogonal polygon-shaped apertures [12, Sec. 2.A]. If $\mathcal{R}^{(i+1)}$ is not tileable and $\widehat{t} \neq T^{(i)}$, skip to the next clustering $(\widehat{t} \rightarrow \widehat{t}+1)$, otherwise (i.e., $\mathcal{R}^{(i+1)}$ turns out to be tileable) set $\hat{\mathbf{c}} \leftarrow \mathbf{c}^{(\widehat{t})}$ and determine the sub-array excitation vector $\widehat{\mathbf{w}}$ by computing the q-th $(q = 1, \ldots, Q^{(i)})$ entry of $\hat{\boldsymbol{\alpha}}(\hat{\boldsymbol{\beta}})$ as the average of the reference *FP* amplitude(phase) coefficients belonging to the $Q^{(i)}$ dominoes placed within $\mathcal{S}^{(i)}$

$$\begin{pmatrix} \hat{\alpha}_q \\ \hat{\beta}_q \end{pmatrix} = \frac{1}{2} \sum_{r=1}^{\widehat{M}+1} \sum_{s=1}^{\widehat{N}+1} \begin{pmatrix} \alpha^{ref}_{\widehat{m}_r \widehat{n}_s} \\ \beta^{ref}_{\widehat{m}_r \widehat{n}_s} \end{pmatrix} \delta_{c_{\widehat{m}_r \widehat{n}_s} q}. \tag{5}$$

Update the equivalent element-level excitations as follows

$$w_{mn} = \begin{cases} \sum_{q=1}^{Q^{(i)}} \hat{\alpha}_q e^{j\hat{\beta}_q} \delta_{c_{mn} q} & \text{if } (x_m, y_n) \in \mathcal{S}^{(i)} \\ \alpha^{ref}_{mn} e^{j\beta^{ref}_{mn}} & \text{if } (x_m, y_n) \in \mathcal{R}^{(i+1)} \end{cases} \tag{6}$$

$(m = 1, \ldots, M;\ n = 1, \ldots, N)$. Given $\hat{\mathbf{c}}$, $\hat{\boldsymbol{\alpha}}$, and $\hat{\boldsymbol{\beta}}$, compute the value of $\widehat{\Phi}$ [$\widehat{\Phi} \triangleq \Phi(\hat{\mathbf{c}}) = \Phi(\mathbf{c}^{(\widehat{t})})$] with (3);

Otherwise, run the *Optimization-Based DCTM* (*O-DCTM*) technique:

- Set the initial ($k = 0$, k being the iteration index) P-size population, $\widehat{\mathbf{C}}^{(k)} = \{\mathbf{c}_p^{(k)};\ p = 1, \ldots, P\}$, according to the schemata-driven strategy in [11];
- Iteratively $(k = 1, \ldots, K-1)$ generate P trial and admissible (i.e., check the "*Admissibility Condition*") clusterings by applying the integer-coded *GA* operators [17], [19]. For each p-th ($p = 1, \ldots, P$) tiling, set $\widehat{t} = (k-1) \times P + p$ and $\hat{\mathbf{c}} \leftarrow \mathbf{c}^{(\widehat{t})}$ to determine $\hat{\boldsymbol{\alpha}}$ and $\hat{\boldsymbol{\beta}}$ as well as $\widehat{\mathbf{w}}$ according to (5) and (6), respectively[2];

- *Step 2.4 - Optimal $\mathcal{S}^{(i)}$-Tiling Selection.* Define the i-th $(i = 1, \ldots, I)$ optimal domino-tiling, $\mathbf{c}^{best}$, as the one with the minimum value of the cost function obtained so far ($\mathbf{c}^{best} = \arg\{\min_{\widehat{t}=1,\ldots,T^{(i)}} [\Phi(\mathbf{c}^{(\widehat{t})})]\}$);
- *Step 2.5 - Sub-Aperture Area Update.* Update the $(i+1)$-th aperture area to be tiled, $\mathcal{R}^{(i+1)} \leftarrow \mathcal{R}^{(i)}$, by removing the pixels covered by the optimal solution found at Step 2.4, $\mathbf{c}^{best}$ (Fig. 5). If the aperture $\mathcal{A}$ is fully tiled (i.e., $i = I$ and $\mathcal{R}^{(i+1)} = \emptyset$), stop the iterative process and output the final array layout, $\mathbf{c}^{opt} = \mathbf{c}^{best}$. Otherwise, increase the *DCTM* iteration index $(i \leftarrow i+1)$, consider the new partition $\mathcal{S}^{(i)}$ to be clustered according to the raster-scan scheme shown in Fig. 2 [e.g., Fig. 5 $(i = 2)$], and goto Step 2.2.

III. NUMERICAL ASSESSMENT

This section is devoted to assess the reliability of the *DCTM* as well as its effectiveness to handle large *PA*s. The first

[2]The number of tilings generated at the i-th $(i = 1, \ldots, I)$ *O-DCTM* iteration is equal to $T^{(i)}_{O-DCTM} = P \times K$, thus the total number of domino-clusterings processed by the *O-DCTM* turns out to be $T_{O-DCTM} = I \times P \times K$.

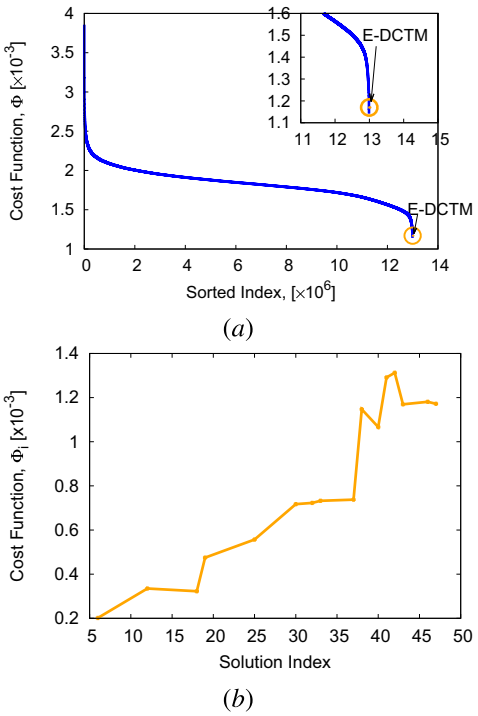

FIGURE 7. *Numerical Validation* ($M = N = 8$, Isotropic Elements, $d_x = d_y = \frac{\lambda}{2}$, $(\theta_0, \phi_0) = (0, 0)$ [deg]) - Behavior of the value of the pattern matching function, Φ, versus (a) the "sorted" solution index t ($1 \le t \le T$) and (b) the *E-DCTM* iteration index i ($i = 1, \ldots, I$; $I = 16$).

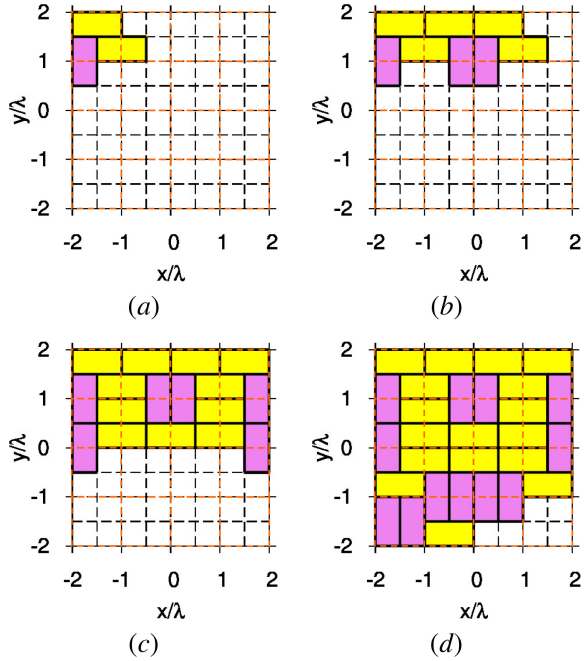

FIGURE 8. *Numerical Validation* ($M = N = 8$, Isotropic Elements, $d_x = d_y = \frac{\lambda}{2}$, $(\theta_0, \phi_0) = (0, 0)$ [deg]; *E-DCTM* - $\widehat{M} \times \widehat{N} = 2 \times 2 \rightarrow I = 16$) - Sketch of $\mathbf{c}^{best}$ at the i-th *E-DCTM* iteration: (a) $i = 1$, (b) $i = 3$, (c) $i = 8$, and (d) $i = 14$.

numerical example is then aimed at validating the *DCTM* by comparing its performance with that one of the *ETM* [11] when tiling small-size *PA*s so that this latter method can be executed in a feasible amount of time. More specifically, a square ($M = N$) array of $M \times N = 8 \times 8$ equally-spaced ($d_x = d_y = \frac{\lambda}{2}$) isotropic (i.e., $\mathbf{g}_{mn}(u, v) = \frac{1}{\sqrt{2}}(\widehat{\mathbf{u}} + \widehat{\mathbf{v}})$; $m = 1, \ldots, M$; $n = 1, \ldots, N$) elements has been considered. By choosing the power pattern mask $\Psi(u, v)$ as in Fig. 6(a), the reference amplitude coefficients, $\boldsymbol{\alpha}^{ref}$, in Fig. 6(*b*) have been computed with the convex programming (*CP*) optimization strategy in [26]. The phase terms have been set to 0 ($\boldsymbol{\beta}^{ref} = \mathbf{0}$) since the mask is symmetric as well as broadside directed, thus real-valued reference excitations are enough for affording the pattern $\mathcal{P}^{ref}(u, v)$ in Fig. 6(*c*), which fulfils the radiation requirements at hand [i.e., $\mathcal{P}^{ref}(u, v) \le \Psi(u, v)$]. The *ETM* [11] has then been applied and the whole set of $T = 1.29 \times 10^7$ different domino-clustered configurations, $\mathbf{C}$, has been generated by computing the corresponding cost function values, $\{\Phi^{(t)} \triangleq \Phi(\mathbf{c}^{(t)}); t = 1, \ldots, T\}$, with (3), as well. Running the *ETM* on a computer equipped with an Intel 2.10 GHz Xeon CPU and 64 Gb of RAM, the global optimal tiling, $\mathbf{c}^{opt}_{ETM}$ ($\mathbf{c}^{opt}_{ETM} = \mathbf{c}^{min}$, $\mathbf{c}^{min} \triangleq \arg\{\min_{t=1,\ldots,T}[\Phi(\mathbf{c}^{(t)})]\}$) [Fig. 9(*b*)], has been found in $\tau_{ETM} \approx 22$ [days]. Figure 7(a) shows the behavior of $\Phi^{(t)}$ (3) versus the solution index sorted from that of the worst tiling $\mathbf{c}^{max}$ ($\mathbf{c}^{max} \triangleq \arg\{\max_{t=1,\ldots,T}[\Phi(\mathbf{c}^{(t)})]\}$) to that of the best one $\mathbf{c}^{min}$, the minimum value of the cost function Φ^{min} [$\Phi^{min} \triangleq \Phi(\mathbf{c}^{min})$] at $\mathbf{c}^{opt}_{ETM}$ being equal to $\Phi^{opt}_{ETM} = 1.14 \times 10^{-3}$. Afterwards, the *E-DCTM* has been used on the same benchmark by setting the size of the partitions, $\{\mathcal{S}^{(i)}; i = 1, \ldots, I\}$, to $\widehat{M} \times \widehat{N} = 2 \times 2$ such that $I = 16$. With reference to a non-optimized software implementation of the procedure detailed in Section II-B, the *E-DCTM* ended in $\tau_{E-DCTM} \approx 28$ [sec] after $T_{E-DCTM} = 47$ ($T_{DCTM} \triangleq \sum_{i=1}^{I} T^{(i)}$) evaluations of the cost function (3) by allowing an impressive computational saving with respect to the *ETM* (i.e., $\frac{\tau_{ETM}}{\tau_{E-DCTM}} \approx 68 \times 10^3$ and $\frac{T_{ETM}}{T_{E-DCTM}} \approx 25 \times 10^3$). More important, the cost function value, Φ^{opt}_{E-DCTM}, of the (*E-DCTM*)-optimized layout, $\mathbf{c}^{opt}_{E-DCTM}$ [Fig. 9(*c*)], turns out to be almost coincident with the global optimum one [i.e., $\Phi^{opt}_{E-DCTM} = 1.17 \times 10^{-3}$ vs. $\Phi^{opt}_{ETM} = 1.14 \times 10^{-3}$ - Fig. 7(a)], the gap being very small (i.e., $\frac{|\Phi_{ETM} - \Phi_{E-DCTM}|}{\Phi_{E-DCTM}} \approx 3\%$). Such a slight deviation is pictorially pointed out by the plots of the corresponding power patterns in Figs. 9(*d*)-9(e) together with theirs cuts along the principal planes, $\phi = 0$ [deg] ($v = 0$) and $\phi = 90$ [deg] ($u = 0$), in Fig. 9(a). For the sake of completeness, the power pattern features, namely the sidelobe level (*SLL*), the peak directivity (*D*), and the half-power beam-width (*HPBW*) along the principal planes for both the *ETM*-tiled arrays and the reference *FP* one are reported in Tab. 1. As it can be inferred, the *SLL* of the *E-DCTM* pattern is 7.05 [dB] higher than that of the reference one, but it deviates only 0.51 [dB] from that of the *ETM* solution (Tab. 1).

As for the behavior of the *E-DCTM* synthesis process, it is interesting to observe in Fig. 7(*b*) that the mask matching metric (3) gets worse during the I loops since the single elementary radiators of the initial *FP* array layout

TABLE 1. *Numerical validation* ($M = N = 8$, isotropic elements, $d_x = d_y = \frac{\lambda}{2}$, $(\theta_0, \phi_0) = (0, 0)$ [deg]) - performance indexes.

	SLL [dB]	D [dBi]	$HPBW_{az}$ [deg]	$HPBW_{el}$ [deg]	Φ [$\times 10^{-3}$]
Reference	-27.78	21.60	16.00	16.00	0.00
ETM	-21.24	21.86	15.44	15.44	1.14
E-DCTM	-20.73	21.85	15.53	15.46	1.17

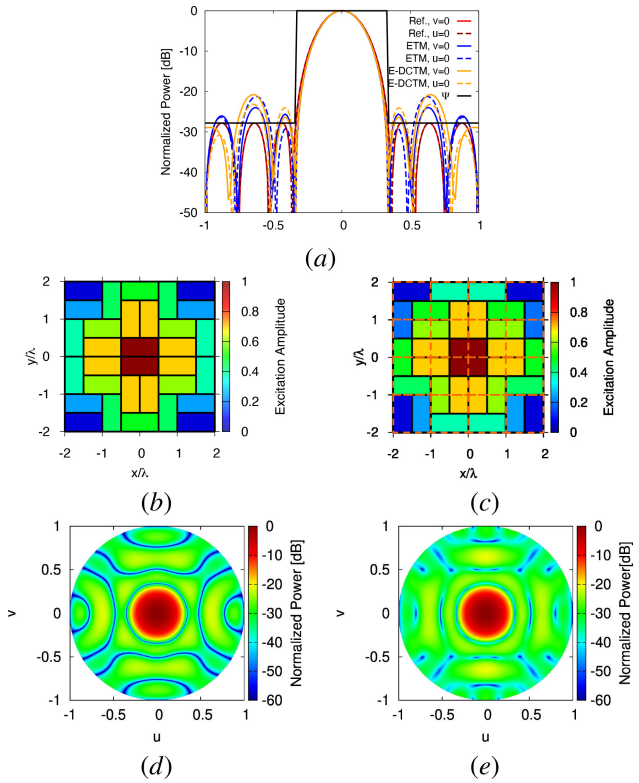

FIGURE 9. *Numerical Validation* ($M = N = 8$, Isotropic Elements, $d_x = d_y = \frac{\lambda}{2}$, $(\theta_0, \phi_0) = (0, 0)$ [deg] [$\rightarrow (u_0, v_0) = (0, 0)$]) - Plots of (a) the normalized power pattern, $\mathcal{P}(u, v)$, along the principal planes $v = 0$ (i.e., $\phi = 0$ [deg]) and $u = 0$ (i.e., $\phi = 90$ [deg]), (*b*)(*c*) the amplitude distribution of the clustered excitations, α, and (*d*)(e) $\mathcal{P}(u, v)$ in the (u, v)-domain Ω synthesized with (*b*)(*d*) the *ETM* and (*c*)(e) the *E-DCTM* ($\widehat{M} \times \widehat{N} = 2 \times 2 \rightarrow I = 16$).

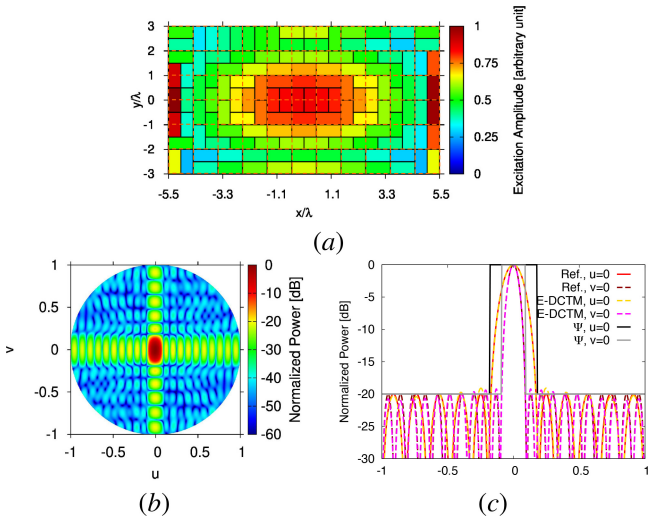

FIGURE 10. *Comparative Assessment* ($M = 22$, $N = 12$, Isotropic Elements, $d_x = d_y = \frac{\lambda}{2}$, $(\theta_0, \phi_0) = (0, 0)$ [deg] [$\rightarrow (u_0, v_0) = (0, 0)$]; *E-DCTM* - $\widehat{M} \times \widehat{N} = 2 \times 2 \rightarrow I = 66$) - Plots of (a) the amplitude distribution of the clustered excitations, α^{opt}_{E-DCTM}, and the corresponding normalized power pattern, $\mathcal{P}^{E-DCTM}(u, v)$, (*b*) in the (u, v)-domain Ω and (*c*) along the principal planes $v = 0$ (i.e., $\phi = 0$ [deg]) and $u = 0$ (i.e., $\phi = 90$ [deg]).

are sequentially replaced by domino clusters as illustrated in Fig. 8.

The second example is aimed at comparing the *DCTM* with other competitive state-of-the-art tiling techniques available in the reference literature. Towards this end, the problem of domino-tiling a rectangular array of $M \times N = 22 \times 12$ elements, addressed in [11], [21], has been selected as benchmark. In [11], [21], the excitations of the *FP* reference array have been defined by considering separable distributions and a Dolph-Chebyshev pattern [5], [27] with $SLL = -20.0$ [dB] to afford a power pattern, $\mathcal{P}^{ref}(u, v)$, with main-lobe pointing towards broadside [i.e., $(u_0, v_0) = (0, 0)$]. For the sake of comparison, while taking into account the trade-off relationship between *SLL* and *HPBW* [5], [6], the power mask $\Psi(u, v)$ has been tailored to force the synthesis of a pattern with *HPBW* values smaller or at most equal to those of the reference solutions in [11], [21] since - unlike (3) - the goal there was the design of a domino-tiled layout with minimum *SLL*. By keeping the same $\mathcal{A}$-partitioning setup of the previous test case (i.e., $\widehat{M} \times \widehat{N} = 2 \times 2$), the layout outputted at the convergence of the *E-DCTM* synthesis is shown in Fig. 10(a) as a color map of the amplitudes of the tiles, $\hat{\boldsymbol{\alpha}}^{opt}_{E-DCTM}$, while the corresponding radiated power pattern in Ω and the pattern cuts along the principal planes are given in Fig. 10(*b*) and Fig. 10(*c*), respectively. It is worth noticing that the *SLL* of the (*E-DCTM*)-tiled array turns out to be very close to that of the solutions in [11], [21] (i.e., $SLL_{E-DCTM} - SLL_{[Anselmi\,2017]} = SLL_{E-DCTM} - SLL_{[Yang\,2021]} = 0.22$ [dB] - Tab. 2) despite the *DCTM* synthesis is not carried out at a time over the whole aperture $\mathcal{A}$. Moreover, once again, the computational cost of the divide and conquer strategy turns out to be lower ($\frac{\tau_{[Anselmi\,2017]}}{\tau_{E-DCTM}} \approx 482$ and $\frac{\tau_{[Yang\,2021]}}{\tau_{E-DCTM}} \approx 1.5$ - Tab. 2).

Open questions in using the *DCTM* are the optimal choice of the partition size, $\widehat{M} \times \widehat{N}$, as well as that of the threshold η_{th} for using either the *E-* or the *O-* version of the *DCTM*. It is clear that these parameters define the trade-off between the overall computational burden and the effective sampling of the T-size solution space (i.e., the possibility to reach the optimal admissible tiling of the array aperture or domino layouts very close to it). On the other hand, they are also strongly connected. In order to derive suitable guidelines for the setup of such calibration parameters, the performance of both the *E-DCTM* and the *O-DCTM* have been evaluated by choosing a square ($M = N$) aperture $\mathcal{A}$ of $M \times N = 24 \times 24$ $\frac{\lambda}{2}$-spaced elements partitioned into I square ($\widehat{M} = \widehat{N}$) sub-areas, while varying η subject to the condition $\frac{\widehat{M}}{M} = \frac{\widehat{N}}{N}$ ($\rightarrow \eta = \frac{\widehat{M}}{M} = \frac{\widehat{N}}{N}$). The power mask $\Psi(u, v)$ has been set as shown in Fig. 12 and the *FP* reference array, whose radiation indexes are reported in Tab. 3, has been generated with the *CP* method [26]. As for the *O-DCTM*, the *GA* control

TABLE 2. *Comparative assessment* ($M = 22$, $N = 12$, isotropic elements, $d_x = d_y = \frac{\lambda}{2}$, $(\theta_0, \phi_0) = (0, 0)$ [deg]) - performance indexes.

	SLL [dB]	D [dBi]	$HPBW_{az}$ [deg]	$HPBW_{el}$ [deg]	Φ [$\times 10^{-5}$]	T	τ [sec]
Reference	−20.00	28.46	4.82	9.13	0.0	-	-
E-DCTM	−19.10	28.52	4.82	9.11	7.77	230	74.6
[Anselmi 2017]	−19.32	28.51	4.82	9.11	-	462×10^3	3.6×10^4
[Yang 2021]	−19.32	28.70	4.82	9.13	-	-	108.8

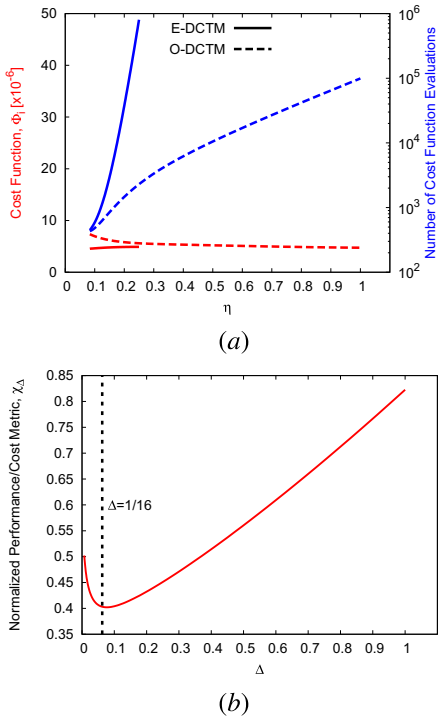

FIGURE 11. *Numerical Assessment* ($M = N = 24$, Isotropic Elements, $d_x = d_y = \frac{\lambda}{2}$, $(\theta_0, \phi_0) = (0, 0)$ [deg]) - Behavior of (a) the optimal value of the pattern matching function, Φ^{opt}, and the number of cost function evaluations, T_{DCTM}, versus η and (*b*) the indicator function χ_Δ versus the partition aspect ratio Δ.

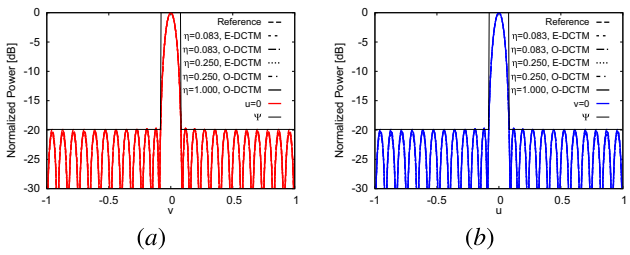

FIGURE 12. *Numerical Assessment* ($M = N = 24$, Isotropic Elements, $d_x = d_y = \frac{\lambda}{2}$, $(\theta_0, \phi_0) = (0, 0)$ [deg] [→ $(u_0, v_0) = (0, 0)$]) - Plots of the normalized power pattern $\mathcal{P}(u, v)$ along (a) the $v = 0$ (i.e., $\phi = 0$ [deg]) and (*b*) the $u = 0$ (i.e., $\phi = 90$ [deg]) planes.

parameters have been set according to [28]: $P = 3 \times \widehat{M} \times \widehat{N}$, $p_c = 0.9$ (p_c being the crossover probability), $p_m = 0.01$ (p_m being the mutation probability), and $K = 1000$ [→ $T^{(i)}_{O-DCTM} = 3000 \times \widehat{M} \times \widehat{N}$ $(i = 1, \ldots, I)$].

The results of such an analysis are summarized in Fig. 11(a) where the behavior of Φ^{opt} and T versus η are reported. By just observing the slope of T_{E-DCTM} in

TABLE 3. *Numerical assessment* ($M = N = 24$, isotropic elements, $d_x = d_y = \frac{\lambda}{2}$, $(\theta_0, \phi_0) = (0, 0)$ [deg]) - performance indexes.

$\widehat{M} = \widehat{N}$	η	SLL [dB]	D [dBi]	$HPBW_{az/el}$ [deg]	[deg]	Φ [$\times 10^{-6}$]	T
Reference							
-	-	−20.00	31.59	4.43	4.43	0.00	-
E-DCTM							
2	$\frac{1}{12}$	−19.71	31.63	4.43	4.43	4.55	448
3	$\frac{1}{8}$	−19.73	31.63	4.43	4.43	4.74	768
4	$\frac{1}{6}$	−19.73	31.63	4.43	4.43	4.91	3672
6	$\frac{1}{4}$	−19.71	31.63	4.43	4.43	4.90	802115
O-DCTM							
2	$\frac{1}{12}$	−19.69	31.66	4.43	4.43	7.34	432
3	$\frac{1}{8}$	−19.69	31.64	4.43	4.43	6.28	509
4	$\frac{1}{6}$	−19.69	31.66	4.43	4.43	5.79	1307
6	$\frac{1}{4}$	−19.72	31.64	4.43	4.43	5.09	2858
8	$\frac{1}{3}$	−19.69	31.65	4.43	4.43	5.76	5020
12	$\frac{1}{2}$	−19.72	31.64	4.43	4.43	4.97	11889
24	1	−19.72	31.64	4.43	4.43	4.74	99161

Fig. 11(a), it is evident that the *E-DCTM* can efficiently handle only very small partitions of $\mathcal{A}$. For instance, the number of cost function evaluations when $\eta = 0.25$ (→ $\widehat{M} \times \widehat{N} = 6 \times 6$ and $I = 3$) is very huge (i.e., $T_{E-DCTM} > 8 \times 10^5$ - Tab. 3). Differently, the *CPU*-time for the *O-DCTM* synthesis is feasible also for wider sub-apertures [i.e., $\eta > 0.25$ - Fig. 11(a)] and the arising tilings (Fig. 14) optimally fulfill the mask constraints ($\Phi^{opt}_{O-DCTM} \leq 6.0 \times 10^{-6}$ - Fig. 12 and Tab. 3). It is also worth pointing out that even when $\eta \leq 0.25$, the *O-DCTM* performs closely to the *E-DCTM* by synthesizing different tiled configurations (Fig. 13), but similar in terms of radiated power patterns (Fig. 12 - Tab. 3). Accordingly, the switching threshold has been set to $\eta_{th} = 0.25$.

As for the calibration of the partitions size, $\widehat{M} \times \widehat{N}$, the following metric

$$\chi_\Delta = \frac{1}{2}\left\{\frac{\Phi^{opt}_\Delta}{\max_\Delta\left[\Phi^{opt}_\Delta\right]} + \frac{T_\Delta}{\max_\Delta[T_\Delta]}\right\} \tag{7}$$

has been considered as an indicator function and its behaviour versus the partition aspect-ratio Δ ($\Delta \triangleq \frac{\widehat{M} \times \widehat{N}}{M \times N}$) has been analyzed. Figure 11(*b*) shows that the minimum of χ_Δ arises when $\Delta = \frac{1}{16}$, thus the value $\Delta^{opt} = \frac{1}{16}$ (→ $(\widehat{M} \times \widehat{N})^{opt} = \frac{M \times N}{16}$) has been chosen for the optimal sizing of the I partitions, $\{\mathcal{S}^{(i)};\ i = 1, \ldots, I\}$, of the aperture $\mathcal{A}$.

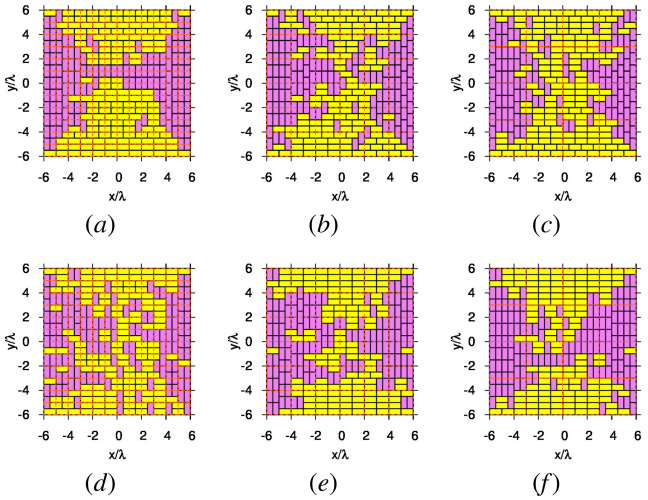

FIGURE 13. *Numerical Assessment* ($M = N = 24$, Isotropic Elements, $d_x = d_y = \frac{\lambda}{2}$, $(\theta_0, \phi_0) = (0, 0)$ [deg]) - Sketch of the domino tiling c^{opt} synthesized with (a)(*b*)(*c*) the *E-DCTM* and (*d*)(e)(*f*) the *O-DCTM* when (a)(*d*) $\eta = \frac{1}{12}$, (*b*)(e) $\eta = \frac{1}{6}$, and (*c*)(*f*) $\eta = \frac{1}{4}$.

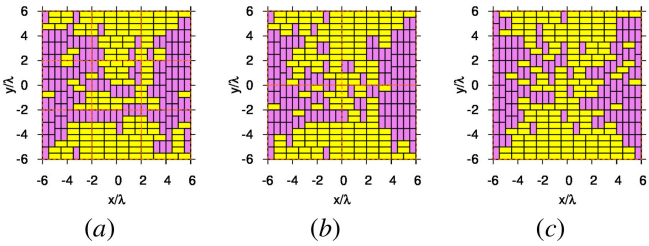

FIGURE 14. *Numerical Assessment* ($M = N = 24$, Isotropic Elements, $d_x = d_y = \frac{\lambda}{2}$, $(\theta_0, \phi_0) = (0, 0)$ [deg]; *O-DCTM*) - Sketch of the domino tiling c^{opt}_{O-DCTM} when (a) $\eta = \frac{1}{3}$, (*b*) $\eta = \frac{1}{2}$, and (*c*) $\eta = 1$.

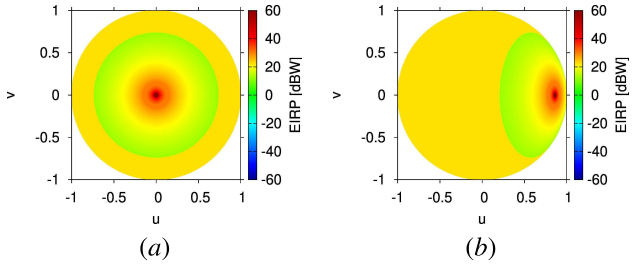

FIGURE 15. *Numerical Assessment* ($M = N = 80$, Directive Elements, $d_x = d_y = 0.52\lambda$) - *ETSI* mask, $\Psi^{ETSI}(u, v)$, when the main-lobe is pointed at (a) broadside (i.e., $(u_0, v_0) = (0, 0) \rightarrow (\theta_0, \phi_0) = (0, 0)$ [deg]) and (*b*) $(u_0, v_0) = (\frac{\sqrt{3}}{2}, 0)$ ($\rightarrow (\theta_0, \phi_0) = (60, 0)$ [deg]).

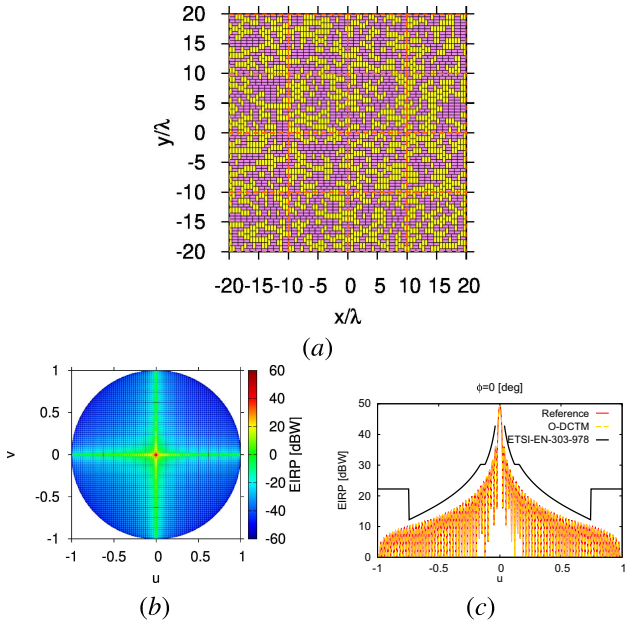

FIGURE 16. *Numerical Assessment* ($M = N = 80$, Directive Elements, $d_x = d_y = 0.52\lambda$, $(\theta_0, \phi_0) = (0, 0)$ [deg] $\rightarrow (u_0, v_0) = (0, 0)$; *O-DCTM* - $\hat{M} \times \hat{N} = 20 \times 20 \rightarrow I = 16$) - Pictures of (a) the sketch of the domino tiling c^{opt}_{O-DCTM} and the corresponding *EIRP* pattern, $E^{O-DCTM}(u, v)$, (*b*) in the (u, v)-domain Ω and (*c*) along the principal planes $v = 0$ (i.e., $\phi = 0$ [deg]) and $u = 0$ (i.e., $\phi = 90$ [deg]).

The next experiments are concerned with the synthesis of very large *PA*s for high-data rate up-link communications between Earth stations on mobile platforms (*ESOMP*) and *LEO* satellites. These antenna systems require a value of the effective isotropic radiated power (*EIRP*) [5], $E(\theta, \phi)$ ($E(u, v) \triangleq \Upsilon \frac{4\pi \mathcal{P}(u,v)}{\int_\Omega \frac{\mathcal{P}(u,v)}{\sqrt{1-u^2-v^2}} du dv}$, Υ being the input power), when pointing towards broadside, $(\theta_0, \phi_0) = (0, 0)$ [deg], greater than 46.0 [dBW] ($E_{dB}(\theta_0, \phi_0) > 46.0$ [dBW], $E_{dB}(\theta_0, \phi_0) \triangleq 10 \times \log[E_{dB}(\theta_0, \phi_0)]$) and the possibility to steer the beam up to $\theta^{max} = 60$ [deg] from broadside. Moreover, the *EIRP* pattern must fit the ETSI EN-303-978 mask [29], $\Psi^{ETSI}(\theta, \phi)$, in the whole scanning cone (i.e., $0 \le \theta \le \theta^{max}$ and $0 \le \phi < 360$ [deg]). For illustrative purposes, the color maps of $\Psi^{ETSI}(u, v)$ when pointing the main beam towards broadside [i.e., $(u_0, v_0) = (0, 0)$] and along $(\theta_0, \phi_0) = (60, 0)$ [deg] [$\rightarrow (u_0, v_0) = (\frac{\sqrt{3}}{2}, 0)$] are shown in Fig. 15(a) and Fig. 15(*b*), respectively.

Given these requirements, the reference *FP* array has been defined to guarantee the absence of grating lobes within the visible range, Ω, whatever the main-lobe pointing direction, and to generate an *EIRP* pattern, $E(\theta, \phi)$, compliant with the *ETSI* masks, $\Psi^{ETSI}(\theta, \phi)$, when steering up to the maximum scan angle ($0 \le \theta \le \theta^{max}$ and $0 \le \phi < 360$ [deg]). Accordingly, the *FP* layout turned out to be composed of $M \times N = 80 \times 80$ elements spaced by $d_x = d_y = 0.52\lambda$ and uniformly fed (i.e., $\alpha^{ref}_{mn} = 1.0$; $m = 1, \ldots, M$; $n = 1, \ldots, N$). Moreover, the (m, n)-th ($m = 1, \ldots, M$; $n = 1, \ldots, N$) phase reference value (5) has been set to

$$\beta^{ref}_{mn} = -\frac{2\pi}{\lambda}(x_{mn}u_0 + y_{mn}v_0). \tag{8}$$

Furthermore, by assuming each (m, n)-th ($m = 1, \ldots, M$; $n = 1, \ldots, N$) radiating element to have an element pattern equal to $\mathbf{g}_{mn}(u, v) = \sqrt[4]{\frac{1-u^2-v^2}{2}}(\hat{\mathbf{u}} + \hat{\mathbf{v}})$, the peak directivity of the reference antenna is equal to $D_{dB} = 40.32$ [dBi] ($D_{dB} \triangleq 10 \times \log D$) at the maximum scan (Tab. 4). Thus, since the *EIRP* pattern is given by $E(\theta, \phi) = \Upsilon \times D(\theta, \phi)$, the value of Υ has been set to $\Upsilon = 4$ [W] (i.e., $\Upsilon_{dB} = 6$ [dBW]) for fulfilling the *ETSI* requirement on the *EIRP*.

Owing to the array size ($M \times N = 6400$ elements), the cardinality of the solution space composed by the whole

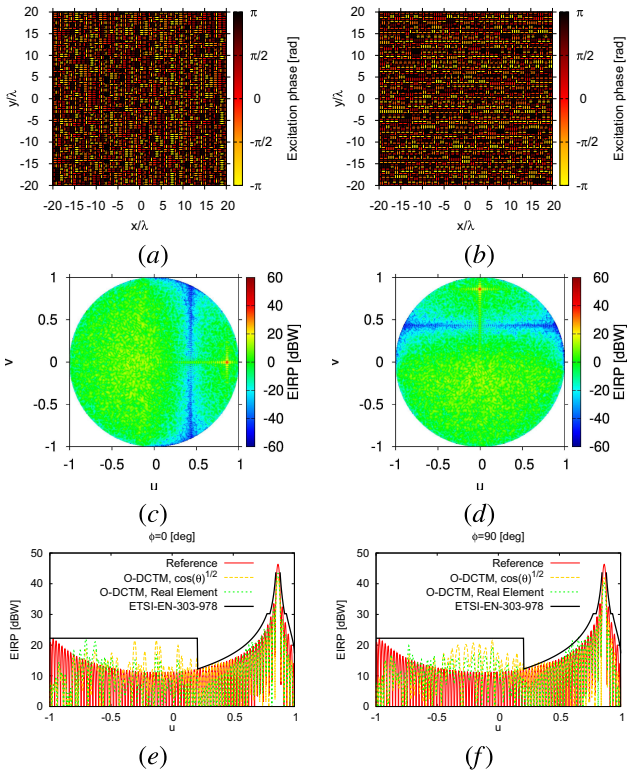

FIGURE 17. *Numerical Assessment* ($M = N = 80$, Directive Elements, $d_x = d_y = 0.52\lambda$; *O-DCTM* - $\widehat{M} \times \widehat{N} = 20 \times 20 \rightarrow I = 16$) - Plots of (a)(*b*) the phase distribution of the clustered excitations, β^{opt}_{O-DCTM}, and the corresponding *EIRP* pattern, $E^{O-DCTM}(u, v)$, (c)(*d*) in the (u, v)-domain Ω and (e)(*f*) along the principal planes $v = 0$ (i.e., $\phi = 0$ [deg]) and $u = 0$ (i.e., $\phi = 90$ [deg]) when pointing the beam towards (a)(*c*)(e) $(u_0, v_0) = (\frac{\sqrt{3}}{2}, 0)$ ($\rightarrow (\theta_0, \phi_0) = (60, 0)$ [deg]) and (*b*)(*d*)(*f*) $(u_0, v_0) = (0, \frac{\sqrt{3}}{2})$ ($\rightarrow (\theta_0, \phi_0) = (60, 90)$ [deg]).

TABLE 4. *Numerical assessment* ($M = N = 80$, directive elements, $d_x = d_y = 0.52\lambda$) - performance indexes.

(θ_0, ϕ_0) [deg]	SLL [dB]	D [dBi]	$EIRP$ [dBW]	$HPBW_{az/el}$ [deg]	[deg]	Φ [$\times 10^{-12}$]
Reference						
$(0, 0)$	-13.30	43.37	49.39	1.22	1.22	0.00
$(60, 0)$	-13.24	40.32	46.34	2.45	1.22	0.00
$(60, 90)$	-13.24	40.32	46.34	1.22	2.45	0.00
O-DCTM						
$(0, 0)$	-13.30	43.37	49.39	1.22	1.22	0.00
$(60, 0)$	-12.52	35.69	41.71	2.52	1.27	7.5
$(60, 90)$	-12.59	35.95	41.97	1.28	2.53	7.7

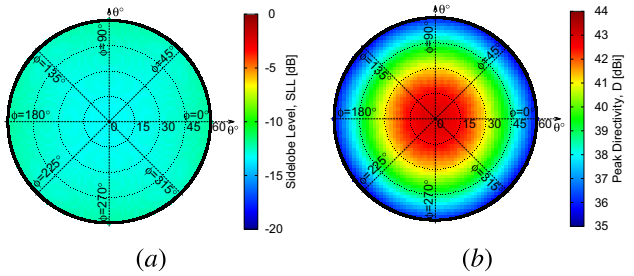

FIGURE 18. *Numerical Assessment* ($M = N = 80$, Directive Elements, $d_x = d_y = 0.52\lambda$; *O-DCTM* - $\widehat{M} \times \widehat{N} = 20 \times 20 \rightarrow I = 16$) - Color map of the (a) *SLL* and (*b*) *D* variations when scanning the beam around the pointing direction $(\theta_0, \phi_0) = (0, 0)$ [deg] within the scanning cone ($0 \le \theta \le \theta^{max}$ and $0 \le \phi < 360$ [deg]).

TABLE 5. *Numerical assessment* ($M = N = 80$, directive elements, $d_x = d_y = 0.52\lambda$; *O-DCTM* - $\widehat{M} \times \widehat{N} = 20 \times 20 \rightarrow I = 16$) - performance statistics.

	Min.	Max.	Avg.	Std-Dev.
SLL [dB]	-13.38	-12.08	-12.79	0.28
D [dBi]	35.46	43.03	39.29	2.14

set of T admissible domino tilings of $\mathcal{A}$ is very huge ($T \ge 1.0 \times 10^{200}$) and an exhaustive search with either the *ETM* or its divide-and-conquer version (*E-DCTM*) as well as the application of the *OTM* [11] would have been computationally unfeasible. Therefore, the *O-DCTM* has been used by setting $\Delta^{opt} = \frac{1}{16}$ so that the size of the partitions of the array aperture resulted $\widehat{M} \times \widehat{N} = 20 \times 20$. In less than 2 days (i.e., $\tau_{O-DCTM} \approx 46$ [hours]), the irregular domino tiled configuration $\mathbf{c}^{opt}_{O-DCTM}$ shown in Fig. 16(a) has been synthesized. Such a layout generates the *EIRP* patterns in Figs. 16(*b*)-16(*c*) towards broadside and those in Fig. 17(*c*)-17(e) and Fig. 17(*d*)-17(*f*) when steering the beam at $(\theta_0, \phi_0) = (60, 0)$ [deg] and $(\theta_0, \phi_0) = (60, 90)$ [deg], respectively. As for these two latter cases, the phase excitations, $\boldsymbol{\beta}^{opt}_{O-DCTM}$, are those depicted in Fig. 17(a) and Fig. 17(*b*), respectively.

As it can be observed in Fig. 16(*c*) and Fig. 17(e)-17(*f*), the *O-DCTM* pattern, $E^{O-DCTM}(\theta, \phi)$, is generally fully compliant with the *ETSI* requirements, while the few violations of the *ETSI* mask, $\Psi^{ETSI}(u, v)$, are almost negligible even along the most challenging scanning directions, the pattern matching error Φ^{opt}_{O-DCTM} being kept below 10^{-11} (i.e., $\Phi^{opt}_{O-DCTM} \approx 7.5 \times 10^{-12}$ - Tab. 4). Moreover, as expected, the performance towards broadside, $(u_0, v_0) = (0, 0)$ [Fig. 16(*c*)], is ideal since there is no phase quantization. In order to further evaluate the beam steering performance, the effect on the sidelobe level, *SLL*, and on the peak directivity, *D*, when scanning the beam around the pointing direction in the whole scanning cone ($0 \le \theta \le \theta^{max}$ and $0 \le \phi < 360$ [deg]) has been analyzed. The color maps shown in Fig. 18 clearly highlight the ϕ-invariant behavior of the radiation performance, the negligible impact on the *SLL* [Fig. 18(a)] and the expected *D* reduction when tilting the beam off-broadside [Fig. 18(*b*)]. For the sake of completeness, the statistics of the *SLL* and *D* values are given in Tab. 5.

In order to assess the matching with the mask when considering realistic element radiators, the wide-band wide-beam slot-coupled radiating element presented in [30] has been scaled to resonate at $f = 29.0$ [GHz] and simulated with the Ansys HFSS full-wave simulator [31]. In order to include mutual coupling effects, the single element pattern has been simulated within a 5×5 array environment. The obtained embedded element factor has been considered for the *EIRP* pattern computation and compared in Fig. 17(e)-(*f*) with the mask and analytic patterns, showing that even

if the pattern deviates from the analytic one, the matching with the mask remains satisfactory.

Beyond the coupling effects, *TRM*s are susceptible of amplitude and phase tolerances that may lead to performance degradation. In order to evaluate the impact of this non-ideality on the radiation pattern of the solution including realistic radiators [30], a Monte Carlo analysis with $J = 10^5$ simulations has been carried out. The tolerances on the excitation amplitudes and phases have been randomly defined within the intervals $[\alpha_q(1-\delta\alpha):\alpha_q(1+\delta\alpha)]$ and $[\beta_q(1-\delta\beta):\beta_q(1-\delta\beta)]$, where $\delta\alpha$ and $\delta\beta$ are the amplitude and the phase tolerance, respectively, set to $\delta\alpha = 0.02$ and $\delta\beta = 3$ [deg] [32]. The plot of the normalized nominal (i.e., error-free) power pattern cut along the $\phi = 90$ [deg] ($u = 0$) plane when pointing the beam toward $(\theta_0, \phi_0) = (60, 90)$ [deg] [Fig. 17(*f*)], compared with the upper, $\mathcal{P}^{sup}(u, v)$, and lower, $\mathcal{P}^{inf}(u, v)$, bounds derived from the Monte Carlo analysis (which represent the "worst cases" for any angle $v \in [-1{:}1]$), is shown in Fig. 19. It can be seen that the power patterns affected by the random errors are in good agreement with the nominal power pattern.

Finally, it is worth pointing out that, analogously to all previous experiments and in general, such an *O-DCTM* domino-tiled layout as well as all others *DCTM*-synthesized array architectures, reduces by half the number of *TRM*s required by its *FP* reference counterpart (i.e., $Q = 3200$ vs. $M \times N = 6400$).

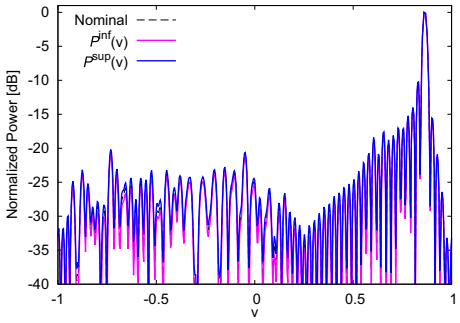

FIGURE 19. *Numerical Assessment* ($M = N = 80$, Directive Elements, $d_x = d_y = 0.52\lambda$; *O-DCTM* - $\widehat{M} \times \widehat{N} = 20 \times 20 \rightarrow I = 16$) - Plot of the normalized nominal power pattern cut along the $u = 0$ (i.e., $\phi = 90$ [deg]) plane when pointing the beam toward $(u_0, v_0) = (0, \frac{\sqrt{3}}{2}) (\rightarrow (\theta_0, \phi_0) = (60, 90)$ [deg]) compared with the upper, $\mathcal{P}^{sup}(u, v)$, and lower, $\mathcal{P}^{inf}(u, v)$, bounds derived from the Monte Carlo analysis.

IV. CONCLUSION

The problem of efficiently designing *PA*s having antenna elements organized into domino clusters and sub-array-only amplitude and phase controls has been addressed by handling large apertures, as well. Towards this end, an innovative domino-tiling method based on a divide-and-conquer strategy has been proposed where the antenna aperture has been subdivided into a set of partitions that have been sequentially tiled, by properly exploiting customized techniques either enumerative or optimization-based, until the complete clustering of the whole array area.

From the numerical assessment, which also include comparisons with state-of-the-art competitive tiling methods, the following main outcomes can be drawn:

- thanks to the partitioning of the array aperture into sub-areas and the use of soft-boundaries, the *DCTM* is able to effectively explore the solution space of the array tilings to find tiled layouts close to the global optimum one with a non-negligible computational saving with respect to other competitive state-of-the-art approaches;
- the *E-DCTM* turns out to be optimal (i.e., it finds the optimal tiled-layout) and computationally-efficient with respect to both the *ETM* and the *OTM* when dealing with small/medium arrays and the condition $\eta_{th} < 0.25$ holds true, while it is unfeasible otherwise;
- thanks to the sequential optimization-driven domino-clustering of the partitions of the array aperture, the *O-DCTM* turns out to be a computationally-scalable and reliable method for tiling large *PA*s.

Future research activities, beyond the scope of this work, will investigate the use of different tile shapes as well as the extension of the *DCTM* to other large aperture geometries of interest in relevant *PA* applications by also including additional manufacturing constraints to simplify the beam-forming network implementation and/or to comply with mechanical features of the installation site (e.g., blockage effects).

ACKNOWLEDGMENT

Andrea Massa wishes to thank E. Vico and L. Massa for their never-ending inspiration, support, guidance, and help.

REFERENCES

[1] J. Wang, V. Manohar, and Y. Rahmat-Samii, "Enabling the Internet of Things with CubeSats: A review of representative beamsteerable antenna concepts," *IEEE Antennas Propag. Mag.*, vol. 63, no. 6, pp. 14–28, Dec. 2021.

[2] J. S. Herd and M. D. Conwey, "The evolution to modern phased array architectures," *Proc. IEEE*, vol. 104, no. 3, pp. 519–529, Mar. 2016.

[3] P. Rocca, G. Oliveri, R. J. Mailloux, and A. Massa, "Unconventional phased array architectures and design methodologies—A review," *Proc. IEEE*, vol. 104, no. 3, pp. 544–560, Mar. 2016.

[4] R. J. Mailloux, S. G. Santarelli, T. M. Roberts, and D. Luu, "Irregular polyomino-shaped subarrays for space-based active arrays," *Int. J. Antennas Propag.*, vol. 2009, Mar. 2009, Art. no. 956524.

[5] R. J. Mailloux, *Phased Array Antenna Handbook*, 3rd ed. Norwood, MA, USA: Artech House, 2018.

[6] R. L. Haupt, *Antenna Arrays—A Computation Approach*. Hoboken, NJ, USA: Wiley, 2010.

[7] M. C. Vigano, G. Toso, G. Caille, C. Mangenot, and I. E. Lager, "Sunflower array antenna with adjustable density taper," *Int. J. Antennas Propag.*, vol. 2009, no. 1, 2009, Art. no. 624035, doi: 10.1155/2009/624035.

[8] Z.-Y. Xiong, Z.-H. Xu, S.-W. Chen, and S.-P. Xiao, "Subarray partition in array antenna based on the algorithm X," *IEEE Antennas Wireless Propag. Lett.*, vol. 12, pp. 906–909, 2013.

[9] P. Rocca, R. J. Mailloux, and G. Toso, "GA-based optimization of irregular sub-array layouts for wideband phased arrays design," *IEEE Antennas Wireless Propag. Lett.*, vol. 14, pp. 131–134, 2015.

[10] P. Angeletti, G. Pelosi, S. Selleri, R. Taddei, and G. Toso, "Unequal polyomino layers for reduced SLL arrays with scanning ability," *Prog. Electromagn. Res*., vol. 162, pp. 31–38, 2018.
[11] N. Anselmi, P. Rocca, and A. Massa, "Irregular phased array tiling by means of analytic schemata-driven optimization," *IEEE Trans. Antennas Propag*., vol. 65, no. 9, pp. 4495–4510, Sep. 2017.
[12] P. Rocca, N. Anselmi, A. Polo, and A. Massa, "Pareto-optimal domino-tiling of orthogonal polygon phased arrays," *IEEE Trans. Antennas Propag*, vol. 70. no. 5, pp. 3329–3342, May 2022.
[13] Y. Ma, S. Yang, Y. Chen, S. Qu, and J. Hu, "Pattern synthesis of 4-D irregular antenna arrays based on maximum-entropy model," *IEEE Trans. Antennas Propag.*, vol. 67, no. 5, pp. 3048–3057, May 2019.
[14] J. Diao, J. W. Kunzler, and K. F. Warnick, "Sidelobe level and aperture efficiency optimization for tiled aperiodic array antennas," *IEEE Trans. Antennas Propag.*, vol. 65, no. 12, pp. 7083–7090, Dec. 2017.
[15] X.-X. Li, W. Dong, Z.-H. Xu, and S.-P. Xiao, "Hierarchical array design strategy composed of irregular and overlapped subarrays in large-scale planar array," *IEEE Trans. Antennas Propag.*, vol. 69, no. 7, pp. 4217–4222, Jul. 2021.
[16] L. W. Mou and Y. J. Cheng, "Design of aperiodic subarrayed phased arrays with structural pepetitiveness," *IEEE Trans. Antennas Propag.*, vol. 70, no. 12, pp. 11697–11706, Dec. 2022.
[17] P. Rocca, N. Anselmi, A. Polo, and A. Massa, "Modular design of hexagonal phased arrays through diamond tiles," *IEEE Trans. Antennas Propag.*, vol. 68, no. 5, pp. 3598–3612, May 2020.
[18] F. A. Dicandia and S. Genovesi, "Wide-scan and energy-saving phased arrays by exploiting Penrose tiling subarrays," *IEEE Trans. Antennas Propag.*, vol. 70, no. 9, pp. 7524–7537, Sep. 2022.
[19] P. Rocca, N. Anselmi, A. Polo, and A. Massa, "An irregular two-sizes square tiling method for the design of isophoric phased arrays," *IEEE Trans. Antennas Propag.*, vol. 68, no. 6, pp. 4437–4449, Jun. 2020.
[20] P. Russo, "Antenna which assures high speed data rate transmission links between satellites and between satellites and ground stations," U.S. Patent 3 262 790, Nov. 16, 1993.
[21] F. Yang et al., "Synthesis of irregular phased arrays subject to constraint on directivity via convex optimization," *IEEE Trans. Antennas Propag.*, vol. 69, no. 7, pp. 4235–4240, Jul. 2021.
[22] F. Yang, Y. Ma, Y. Chen, S. Qu, and S. Yang, "A novel method for maximum directivity synthesis of irregular phased arrays," *IEEE Trans. Antennas Propag*., vol. 70, no. 6, pp. 4426–4438, Jun. 2022.
[23] S. Karademir, O. A. Prokopyev, and R. J. Mailloux, "Irregular polyomino tiling via integer programming with application in phased array antenna design," *J. Glob. Optim.*, vol. 65, pp. 137–173, Jun. 2016.
[24] S. Desreux and E. Remila, "An optimal algorithm to generate tilings," *J. Discrete Algorithms*, vol. 4, no. 1, pp. 168–180, 2006.
[25] W. P. Thurston, "Conway's tiling groups," *Amer. Math. Month.*, vol. 97, no. 8, pp. 757–773, Oct. 1990.
[26] O. M. Bucci, L. Caccavale, and T. Isernia, "Optimal far-field focusing of uniformly spaced arrays subject to arbitrary upper bounds in nontarget directions," *IEEE Trans. Antennas Propag.*, vol. 50, no. 11, pp. 1539–1554, Nov. 2002.
[27] R. S. Elliott, *Antenna Theory Design*. Hoboken, NJ, USA: Wiley, 2003.
[28] P. Rocca, M. Benedetti, M. Donelli, D. Franceschini, and A. Massa, "Evolutionary optimization as applied to inverse scattering problems," *Inverse Probl.*, vol. 24, pp. 1–41, Nov. 2009.
[29] *Satellite Earth Stations and Systems (SES); Harmonised Standard for Earth Stations on Mobile Platforms (ESOMP) Transmitting Towards Satellites in Geostationary Orbit, Operating in the 27,5 GHzto 30,0 GHz Frequency Bands Covering the Essential Requirements of Article 3.2 of the Directive 2014/53/EU*, ETSI Stanadard 303 978 V2.1.2 (2016-10), 2016. Accessed: May 23, 2023. [Online]. Available: http://www.etsi.org
[30] M. Salucci, G. Oliveri, M. A. Hannan, R. Azaro, and A. Massa, "Wide-band wide-beam circularly-polarized slot-coupled antenna for wide-angle beam scanning arrays," *Sensors*, vol. 23, no. 3, p. 1123, 2023.
[31] *ANSYS Electromagnetics Suite-HFSS*, ANSYS, Canonsburg, PA, USA, 2021.
[32] B. Sadhu et al., "A 28-GHz 32-element TRX phased-array IC with concurrent dual-polarized operation and orthogonal phase and gain control for 5G communications," *IEEE J. Solid-State Circuits*, vol. 52, no. 12, pp. 3373–3391, Dec. 2017.

NICOLA ANSELMI (Senior Member, IEEE) received the Master Degree in Telecommunication Engineering from the University of Trento, Italy, in 2012, and the Ph.D. degree from the International Doctoral School in Information and Communication Technology, Trento, Italy, in 2018. From 2020 to 2025 he was Assistant Professor at the Department of Civil, Environmental, and Mechanical Engineering (DICAM) at the University of Trento, and since 2018 he has been a Research Fellow of the ELEDIA Research Center. Since 2026, he has been a tenured Researcher at the Institut d'Électronique et des Technologies du Numérique (IETR), at the University of Rennes, France, as the holder of the "Chaire de Recherche de Rennes Metropole."

Dr. Anselmi is a member of the IEEE Antennas and Propagation Society, he serves as an Associate Editor of the IEEE Antennas and Wireless Propagation Letters and of the IEEE Open Journal of Antennas and Propagation, and as a reviewer for different international journals including IEEE Transactions on Antennas and Propagation, IEEE Antennas and Wireless Propagation Letters, and IET on Microwaves, Antennas & Propagation. His research activities are mainly focused on synthesis methods for unconventional antenna array architectures, tolerance analysis of antenna systems, and electromagnetic inverse scattering techniques.

In 2023 Dr. Anselmi received the Italian National Scientific Qualification for the position of Full Professor, and in 2019 the Qualification aux fonctions de maître de conférences. Moreover, he has been the recipient of the "Giorgio Barzilai" award for Young Researchers by the Italian Electromagnetic Society (SIEM) in 2016, of the "Young Scientist" Prize by the Applied Computational Electromagnetics Society (ACES) in 2018, and of the "Mini-Circuits Harvey Kaylie Best Paper Prize" by the IEEE International Conference on Microwaves, Communications, Antennas & Electronic Systems (COMCAS) in 2019.

PAOLO ROCCA (Fellow, IEEE) received the M.S. degree (summa cum laude) in telecommunications engineering and the Ph.D. degree in information and communication technologies from the University of Trento, Italy, in 2005 and 2008, respectively.

He is currently an Associate Professor with the Department of Civil, Environmental, and Mechanical Engineering, University of Trento, a Huashan Scholar Chair Professor with Xidian University, Xi'an, China, and a member of the ELEDIA Research Center. He has been a visiting Ph.D. student with Pennsylvania State University, USA, and the University Mediterranea of Reggio Calabria, Italy, and a Visiting Researcher with the Laboratoire des Signaux et Systems (L2S@ Supelec), France, in 2012 and 2013. He has been an Invited Professor with the University of Paris Sud, France, in 2015 and the University of Rennes 1, France, in 2017. He published six book chapters, more than 500 scientific publications among which more than 180 in international journals and more than 320 in national and international conferences where he presented more than 50 invited contributions. He has organized more than 35 scientific sessions in international conferences and has participated to several technological projects in the international and European framework as well as at the national and local levels with national agencies. His main interests are in the framework of computational electromagnetics with focus on antenna array synthesis and analysis, electromagnetic inverse scattering, and artificial intelligence techniques and quantum computing methods as applied to electromagnetics.

Prof. Rocca has been awarded from the IEEE Geoscience and Remote Sensing Society and the Italy Section with the Best Ph.D. Thesis Award IEEE-GRS Central Italy Chapter. He received the National Scientific Qualification for the position of Full Professor in Italy and France in April 2017 and January 2020, respectively. He served as an Associate Editor for the IEEE ANTENNAS AND WIRELESS PROPAGATION LETTERS from 2011 to 2016 and the *Microwave and Optical Technology Letters* from 2019 to 2020 and has been serving as an Associate Editor for the *IEEE Antennas and Propagation Magazine* since 2020 and *Engineering* since 2020. He is a member of the Big Data and AI Working Group for the Committee on Engineering for Innovative Technologies of the World Federation of Engineering Organizations.

GIOVANNI TOSO (Fellow, IEEE) received the Laurea degree (cum laude), the Ph.D. degree, and the Postdoctoral Fellowship from the University of Florence, Italy, in 1992, 1995, and 1999, respectively. During his Ph.D. and Post-Doc, he spent more than one year as a Visiting Scientist with the Laboratoire d'Optique Electromagnetique, Marseille, France. In 1999, he was a Visiting Scientist with the University of California at Los Angeles. In 2000, he received a scholarship from Alenia Spazio, Rome, Italy. In 2000, he was appointed Researcher with the Radio Astronomy Observatory, Italian National Council of Research (CNR). Since 2000, he has been with the Antenna and Submillimeter Waves Section, European Space Agency (ESA), European Space Research and Technology Centre, Noordwijk, The Netherlands. He has been initiating several research and development activities on satellite antennas based on arrays, reflectarrays, discrete lenses, and reflectors. In particular, in the field of onboard satellite antennas, he has been coordinating activities on multibeam antennas (active and passive) mainly for Telecom applications. In the field of terminal antennas, he has been supporting the development of reconfigurable antennas with electronic, mechanical, and hybrid scanning; some of these antennas are now available as products. He has promoted the development of the commercial software tool QUPES by TICRA, now used worldwide, for the analysis and design of periodic and quasi-periodic surfaces, such as reflectarrays, frequency-selective surfaces, transmitarrays, and polarizers. He received, together with Prof. A. Skrivervik, the European School of Antennas (ESoA) Best Teacher Award in 2018. In 2014, he was the Guest Editor, together with Dr. R. Mailloux, of the Special Issue on "Innovative Phased Array Antennas Based on Non-Regular Lattices and Overlapped Subarrays" published in the IEEE TRANSACTIONS ON ANTENNAS AND PROPAGATION, and for the same society, he was an Associate Editor from 2013 to 2016. In 2018, he was the Chairperson of the 39th ESA Antenna Workshop on "Multibeam and Reconfigurable Antennas." Since 2010, together with Dr. P. Angeletti, he has been instructing short courses on Multibeam Antennas and Beamforming Networks during international conferences, such as IEEE Antennas and Propagation Society, IEEE MTT International Microwave Symposium, IEEE International Conference on Wireless Technology and Systems, European Conference on Antennas and Propagation, and European Microwave Week, that have been attended by more than 1000 participants. He is the Organizer of the ESoA course on Active Antennas. Since January 2023, he has been elevated to IEEE Fellow grade for contributions to multibeam antenna developments for satellite applications.

ANDREA MASSA (Fellow, IEEE) has been a Full Professor of Electromagnetic Fields with the University of Trento since 2005. He is currently the Director of the Network of Federated Laboratories "ELEDIA Research Center" located in Brunei, China, Czech, Ethiopia, France, Greece, Italy, Japan, Per, and Tunisia, with more than 150 researchers. Moreover, he is a Holder of a Chang-Jiang Chair Professorship with the University of Electronic Science and Technology of China (UESTC), Chengdu, China, a Visiting Research Professor with the University of Illinois at Chicago, Chicago, USA, a Distinguished Visiting Professor with Tsinghua University, Beijing, China, a Visiting Professor and an IAS Distinguished Scholar with Tel Aviv University, Tel Avivndrea Massa, Israel, and a Professor with CentraleSupelec, Paris, France. He has been a Holder of a Senior DIGITEO Chair with L2SCentraleSupelec and CEA LIST in Saclay, France, a UC3M-Santander Chair of Excellence with the Universidad Carlos III de Madrid, Spain, an Adjunct Professor with Penn State University, USA, a Guest Professor with UESTC, and a Visiting Professor with the Missouri University of Science and Technology, USA; the Nagasaki University, Japan; the University of Paris Sud, France; Kumamoto University, Japan; and the National University of Singapore, Singapore. He published more than 900 scientific publications among which more than 350 in international journals (>17 000 citations—H-index = 69 [Scopus]; >14 000 citations—H-index = 63 [ISI WoS]; >28 000 citations—H-index = 95 [Google Scholar]) and more than 570 in international conferences, where he presented more than 210 invited contributions (>50 invited keynote speaker). He has organized more than 100 scientific sessions in international conferences and has participated to several technological projects in the national and international framework with both national agencies and companies (18 international prj, >5 MEu; 8 national prj, >5 MEu; 10 local prj, >2 MMEu; 63 industrial prj, >10 MEu; and 6 university prj, >300 KEu). His research activities are mainly concerned with inverse problems, antenna analysis/synthesis, radar systems and signal processing, cross-layer optimization and planning of wireless/RF systems, system-by-design and material-by-design (metamaterials and reconfigurable materials), and theory/applications of optimization techniques to engineering problems (coms, medicine, and biology). He was appointed as an IEEE AP-S Distinguished Lecturer from 2016 to 2018 and served as an Associate Editor for the IEEE TRANSACTION ON ANTENNAS AND PROPAGATION from 2011 to 2014. He is an IET Fellow and an Electromagnetic Academy Fellow.